

Large Scale Synthesis of Colloidal Si Nanocrystals and their Helium Plasma Processing into Spin-On, Carbon-Free Nanocrystalline Si Films

*Pratyasha Mohapatra^a, Deyny Mendivelso-Perez^b, Jonathan M. Bobbitt^b, Santosh Shaw^a, Bin Yuan^c, Xinchun Tian^a, Emily A. Smith^{bd}, and Ludovico Cademartiri^{*acd}*

a. Department of Materials Science & Engineering, Iowa State University of Science and Technology, 2220 Hoover Hall, Ames, IA, 50011.

b. Department of Chemistry, Iowa State University of Science and Technology, Gilman Hall, Ames, IA, 50011

c. Department of Chemical & Biological Engineering, Iowa State University of Science and Technology, Sweeney Hall, Ames, IA, 50011

d. Ames Laboratory, U.S. Department of Energy, Ames, IA, 50011

KEYWORDS: colloidal nanoparticle, large scale synthesis, nanocrystalline Si film, helium plasma, carbon free

ABSTRACT: This paper describes a simple approach to the large-scale synthesis of colloidal Si nanocrystals and their processing into spin-on carbon-free nanocrystalline Si films. The synthesized silicon nanoparticles are capped with decene, dispersed in hexane and deposited on silicon substrates. The deposited films are exposed to non-oxidizing room temperature He plasma to remove the organic ligands without adversely affecting the silicon nanoparticles, to form crack free thin films. We further show that the Reactive Ion Etching (RIE) rate in these films is 1.87 times faster than for single crystalline Si, consistent with a simple geometric argument that accounts for the nanoscale roughness caused by the nanoparticle shape.

Silicon is abundantly available and is the bedrock of the semiconductor industry. Silicon wafers cut from single crystalline silicon (sc-Si) are used for substrates, for photochemical cells,¹ and are used ubiquitously in the semiconductor industry for manufacturing microchips.² Nonetheless, sc-Si has limitations: (i) its fabrication is cumbersome and costly, due to complexity, high temperatures, and significant material loss;³ (ii) its solar conversion efficiency (i.e., solar energy to electrical energy) in photovoltaic cells is limited to 18%-24% (for commercial solar cells) depending on fabrication and material quality;^{4,5} (iii) its indirect band gap (1.12eV) makes its application in optoelectronic devices challenging.⁶ These limitations have prompted the search for alternatives. Polycrystalline silicon has much lower manufacturing costs, but has lower solar conversion efficiency.⁷ Thin films of amorphous silicon (a-Si) and nanocrystalline silicon (nc-Si) deposited by chemical vapor deposition (CVD) or sputtering are another option. They have a larger band gap (between 1.4 and 2.5 eV⁸⁻⁹) and a higher absorption coefficient than crystalline silicon,⁹ but the manufacturing and material costs are, in general, lower than for the production of sc-Si wafers and they are much easier to process. A-Si has been widely used in semiconductor thin film technology due to its different properties (e.g., photoluminescence) and ease of processing, but the

dangling bonds in its structure are detrimental to the band gap and must be passivated with hydrogen.¹⁰ Even after passivation, a-Si still suffers from a high defect density.⁸ nc-Si has short range crystalline order and consists of nanosize grains surrounded by amorphous Si.¹¹⁻¹² While still defective, nc-Si displays interesting properties (e.g., size tunable photoluminescence below 5nm¹³⁻¹⁹) associated with the nanoscale size of the crystalline grains.

Thin film applications have also been hindered by limitations of the available processing strategies. (i) Thin film solar cells have low energy conversion efficiency, which degrades under extended exposure to light through Light-Induced Degradation (LID) mechanisms,²⁰ which are especially serious in the case of amorphous Si.¹⁰ (ii) The formation of the nanostructure depends very strongly on the fabrication and processing conditions,^{14, 21-23} which complicates the predictive control of the crystallite shape and size. (iii) The manufacturing process generally uses CVD or sputtering, which require high vacuum conditions that are cost intensive, and use gases, like silane, SiH₄, that are serious safety hazards.

The fabrication of nc-Si thin films from colloidal Si nanoparticles could eliminate some of these issues. Firstly, the nucleation and growth of the crystalline grains is performed before the deposition of the material, which allows, in principle, for a higher crystallinity and a much better control over size and shape of the crystalline grains. Furthermore, if the ligands are removed by a low-temperature process (e.g., ligand stripping, plasma processing), this approach could preserve the size and shape of the nanocrystalline building blocks, and could be applied to thermally sensitive substrates (e.g., polymer films, fibers).

In spite of this potential, the creation of spin-on nc-Si films from colloidal nanoparticles has not been heavily investigated for two main reasons: (i) the difficulty of producing colloidal nanocrystals of Si in sufficient amounts and with sufficient colloidal stability to produce spin-on

films;^{14, 24} (ii) the difficulty of removing completely the ligands from the deposited films and to do so without compromising their structural integrity.²⁵⁻²⁶ In this paper we resolve both of these problems by developing a large scale synthesis approach to Si nanoparticles, and by using He plasma processing to remove the ligands at low temperatures, resulting in crack-free nanocrystalline Si films.

We are interested²⁷⁻²⁹ (like others³⁰⁻⁴⁴) in the synthesis of materials that uses colloidal nanoparticles as building blocks. This approach to the fabrication of nanostructured inorganic materials typically employs calcination in oxygen to remove the organic ligands.⁴⁵ Our results showed that calcination leaves behind substantial amounts of the original carbon.⁴⁶ Furthermore, calcination in oxygen is incompatible with oxygen-sensitive phases (e.g., most semiconductors) and causes grain growth.

In our approach, instead, low pressure (100 to 2000 mTorr), low temperature (~40-60°C) plasmas successfully remove all the ligands from **Colloidal Nanocrystal Assemblies** (CNAs) without causing coarsening of the nanocrystalline building blocks.^{29, 46-48} If the CNAs are disordered and thinner than ~450 nm, the ligands can be removed completely without causing cracks in the CNA.²⁸ If He is used as a feed gas, the ligands can be removed from oxygen-sensitive nanocrystals.⁴⁹ The result of this approach is an all-inorganic, single phase, crack-free solid state material, whose microstructure is defined by the original nanoparticle building blocks.^{27, 29}

We here demonstrate the application of this approach to the fabrication of nanocrystalline Si coatings by the processing of spin-on films of colloidal Si nanoparticles with He/H₂ plasma. We find that the reactive ion etching (RIE) rate (18:10:10.6 SCCM for SF₆:O₂:Ar; 10W power at 10 mTorr) on the ligand-free films is approximately 1.87 times faster than in single crystal Si, consistently with the nanoscale roughness caused by the nanoparticle shape. These data suggest

that while plasma etching of the ligands occurs homogeneously throughout the CNAs²⁹ thanks to the diffusion of excited species in the pores of the CNA, RIE only acts on the top surface of the film.

Synthesis of the colloidal Si nanocrystals

Silicon nanoparticles are synthesized using different techniques, such as pulsed laser ablation (PLA),⁵⁰⁻⁵² attrition ball milling,⁵³ laser irradiation of silanes,⁵⁴ chemical reduction of silicon hydride,⁵⁵ plasma synthesis,^{14, 21, 56} or thermal decomposition/disproportionation.^{16, 57} We adopted a thermal processing approach (cf. Figure 1) due to its simplicity, and we modified it to reduce its safety issues,⁵⁸⁻⁵⁹ and improve its scalability⁵⁹ and the quality of the product. The protocol is based on the route developed by G.A. Ozin and colleagues,⁵⁹ and on the basis of pioneering work by J. Veinot and colleagues.^{16, 57} Briefly, there are five steps. **(i) Disproportionation.** SiO powder is annealed at high temperature in a reducing atmosphere to produce Si nanocrystals in an amorphous matrix of SiO and SiO₂. **(ii) Etching.** The oxide is etched by an aqueous etchant solution under a flow of inert gas. **(iii) Separation.** The liberated nanocrystal are spontaneously transferred into a water-immiscible terminal alkene solution. **(iv) Hydrosilylation.** The dispersion of hydrogenated nanocrystals in the alkene is heated to induce hydrosilylation, resulting in ligand-capped nanoparticles. **(v) Purification.** The colloidal dispersion is then purified by repeated exposure to polar solvents, centrifugation, and redispersion in apolar solvents.

We now discuss the design of each of these steps.

Crystallization of Si from SiO. Commercial silicon monoxide powder (SiO, -325 mesh, from Sigma Aldrich) was used as the starting material, as it is rich in Si, inexpensive (<2 \$/g), and readily available in bulk. Silicon monoxide is a unique stoichiometry of silicon oxide with an

implicit oxidation state for silicon of +2. The annealing of amorphous SiO powder in a reducing atmosphere results in its disproportionation into Si and SiO₂ and the crystallization and growth of the Si regions. There is significant disagreement on the exact chemical structure of SiO and whether the commercially available powder is a unique compound or a mixture of SiO₂ and Si. Spectroscopic studies have shown that the commercially available powder cannot be a inhomogeneous mixture,⁶⁰ consistently with prior thermochemical analyses⁶¹ and XRD characterization.⁶² On the other hand ²⁹Si-MAS-NMR spectroscopy,⁶³ XANES spectroscopy,⁶³ Transmission Electron Microscopy,⁶⁴⁻⁶⁵ X-ray scattering,⁶⁵ Atom Probe Tomography,⁶⁶ and computer simulations came to the opposite conclusion: while the material is not a composite, it is inhomogeneous.⁶⁵ The large volume fraction (20-25%⁶⁴) occupied by the interphase domains composed of suboxide-type (SiO_x) tetrahedral structures⁶⁵ could explain why SiO shows a significantly larger heat of combustion than mixtures of SiO₂ and Si.^{61, 67} If the theoretical prediction that SiO is thermodynamically unstable against disproportionation⁶⁷ is correct, it is possible that the discrepancies in the experimental conclusions arise from different processing histories of the samples.

The SiO powder was placed in a tube furnace, which was then purged with a 5% H₂ : 95% Ar mixture for 1 hr. The powder was heated to a designated temperature (900°C, 1000°C and, 1100°C, 20°C/min) under a continuous flow of gas, held for a specified time (1, 2, 3, 5 and 10 hr) and then cooled down to room temperature naturally (2-3°C/min).⁶⁸⁻⁶⁹

The annealed powders show a significantly darkened color indicating the formation and growth of the Si phase. The X-ray Diffraction (XRD) patterns of the starting SiO powders, as well as those annealed at 1000°C for times ranging between 1 and 10 hours are shown in Figure 1b (annealing at 900°C did not yield visible Si peaks in the XRD spectrum indicating that the temperature was

not sufficient to form Si nanoparticles crystalline enough to be detected by XRD). A crystalline phase emerges after 1 hr of annealing at 1000°C and is characterized by reflections at 28.4°, 47.7°, and 55.8°, which are consistent with the (111), (220), and (311) planes of Si. The broad peak at ~23° is attributed to amorphous SiO₂/SiO. As the annealing temperature and holding time are increased, the peaks associated with Si change somewhat over time. The overall fraction of the crystalline Si phase did not change significantly over time (the linear fit of the fractional area of the (111) reflection vs processing time had a slope of $0.003 \pm 0.003 \text{ hr}^{-1}$). The breadths of the peaks instead did change indicating the growth of the crystallites. The diameter was estimated before liberation from the amorphous matrix by XRD through a Scherrer analysis on the (111) peak, after background subtraction, and assuming a spherical shape for the nanoparticles.⁷⁰⁻⁷¹ The results (cf. Figure 1c, black scatters) indicate a slow change in particle size with processing time from 3.4 ± 0.2 nm to 4.5 ± 0.3 nm. The size estimation was later confirmed by TEM analysis on the liberated particles (cf. Figure 1c, red scatters).

Etching the amorphous matrix. The matrix has to be selectively removed without damaging the Si nanocrystals. The typical approach is to use an HF-based etchant solution^{18, 59} since it etches both SiO₂ and SiO. The reported protocol used an etching mixture consisting of 95 vol% EtOH and 48% HF in a 1:2 volume ratio.⁵⁹ To increase the scale of the synthesis, reduce the risk profile, and have a slower and more controllable etch, we made three changes: we degassed the solvents before etching, we conducted the etching under Ar flow, and we substituted the 48% HF solution with a 6 mol% ammonium bifluoride (NH₄HF₂) solution in deionized (DI) water. Oxidation during etching is one of the major causes of reduction of yield in this reaction. Therefore, oxygen must be removed from the solvents and from the atmosphere. The Ar flow also helps displacing the SiF₄ etching byproduct from the liquid/air interface, therefore accelerating the reaction kinetics.

Ammonium bifluoride is a white crystalline solid, and is safer to handle and store than 48% HF solution. In water, ammonium bifluoride spontaneously dissociates to form NH_4^+ and HF_2^- and partially reacts with H_2O to form $2\text{HF} + \text{OH}^-$. The etching reaction with SiO_2 is summarized as:



where NH_4F and H_2O remain in solution and SiF_4 leaves the system as a gas. Six hours of etching were sufficient to remove any visible trace of the oxide from the product, according to TEM characterization.

Hydrosilylation. The Si nanoparticles liberated from the silica matrix are hydride terminated (ncSi:H) and must be colloidally stabilized by grafting organic ligands to the surface by hydrosilylation with terminal alkenes. 100 ml of 1-decene was added to 200 ml of aqueous etchant solution after the etching time and stirred for 5 mins under an Ar atmosphere. The organic phase was then heated at 170°C for 20 hours for hydrosilylation to occur and to generate decyl-capped Si nanocrystals,⁷² which are then dispersible in non-polar organic solvents like hexane and toluene.

TEM analysis (cf. Fig 1d) shows that the Si nanoparticles are well dispersed, nearly spherical, and relatively monodisperse. The size of the liberated particles measured by TEM agrees with the values obtained from XRD prior to etching, indicating that the etching, separation, and hydrosilylation steps do not seem to have a very significant effect on particle size. The TEM analysis allows to quantify the polydispersity which decreases somewhat from 25% after ~2 hrs at 1000°C to 19% after ~10 hrs at 1000°C . This is consistent with modeling of ensembles of nanocrystals growing by Ostwald ripening, which suggested that the growth leads to a stationary value of polydispersity of approximately 20%.⁷³

Formation of thin films by spin coating

The dispersion of colloidal Si nanocrystals in organic solvents (like hexane) can be spin-coated to form colloidal nanocrystal assemblies (CNAs), from which the ligand can then be removed by plasma processing (cf. Figure 2). The Si nanoparticles dispersed in hexane was first deposited on a silicon substrate. Spin-coating of the thin film was conducted on a spin-coater (Laurell Technologies Model: WS-650MZ-23NPP) by accelerating the substrate at 330 rpm/s to 1000 rpm to spread the dispersion evenly on the substrate forming a flat surface. The film is then held at 1000 rpm for 25 s to dry out the solvent. CNAs ranging in thickness between 160nm and 570nm were obtained by controlling the concentration of the dispersion. Concentrations in the range of 100 mg/ml are necessary to form films in this range of thicknesses. The thickness of the deposited films depends on the type of solvent, concentration of the dispersion and the spin coating parameters. We controlled the thickness by altering the concentration of the dispersion while keeping the spin parameters fixed, for better comparison and reproducibility. As we previously showed for a number of dispersions of nanocrystals, disordered CNAs can tolerate a complete ligand removal by plasmas without cracking.²⁸ The formation of disordered films was associated with the choice of solvents. Importantly, it was found that poor colloidal stability was not a necessary condition for the formation of disordered films. Solvents (like hexane) with low values of the Hansen solubility parameter δ_p , reproducibly led to disordered spin-coated films that resisted cracking.²⁸ Also in this case, spin-coating dispersions of Si nanocrystals in hexane yielded crack-free films. The quality of the films depended very strongly on the purification of the dispersion. The presence of incompletely etched material or free decene yielded films with a number of defects ranging from surface roughness, to striations, to comets. Furthermore, our current understanding

indicates that the effectiveness of plasma processing in removing the ligands relies on the porosity of the deposited CNA and therefore on the absence of free ligands.

Plasma treatment of spincoated Si nc thin films

We removed the organic decyl ligands by exposing the deposited silicon films to low temperature plasma. Both He and 5% H_2 /95%He were used as feed gases to avoid oxidation. Plasma feed gases such as Ar and N_2 were not used due to issues such as reaction/implantation⁷⁴ and sputtering.⁷⁵ The deposited thin films were exposed to a 500 mTorr, 30W, He plasma for 24 hours. The thickness of the films after ligand removal was between 35 and 220 nm, depending on the initial thickness and volume fraction of ligands. The large volume loss did not cause the film to crack, consistent with our prior findings for disordered CNAs thinner than 450nm (cf. Figure 2b).²⁸

We verified the removal of ligands by comparing the Raman spectra of the unprocessed and plasma processed (24hr, 95% He/5% H_2) thin films (cf. Fig 2c). While Raman spectroscopy is poorly suited to the characterization of residual carbon after calcination (due to the formation of amorphous carbon), the integral of the four peaks from 2850-2990 cm^{-1} corresponding to the C-H bond stretching do correlate with carbon concentration during plasma processing.⁴⁹ A peak observed at 1290 cm^{-1} (not shown) corresponds to the Si- CH_3 stretch in silanes and suggests the hydrosilylation of the nanoparticles by decene. Plasma processing causes all of these peaks to disappear, suggesting a complete removal of the C-H and Si-CH bonds in the plasma processed films.

As shown in a prior publication, differently from calcination, where the complete elimination of C-H Raman scattering signal can occur without the complete removal of carbon from the system,

the reduction in the C-H Raman scattering signal in plasma processing is monotonically (albeit not linearly) correlated with the amount of carbon in the film. Therefore, this data confirms that ligands can be fully removed from the films.

Ion beam analysis, a useful tool that we used in prior publications to directly measure carbon residue after plasma processing, could not be used effectively in this instance because of the use of a Si substrate underneath the Si CNA. We used Si substrate to ensure consistency with our prior experiments since substrate composition and electrical properties can affect plasma behavior in proximity to the surface.^{28, 46}

Reactive ion etching

Given the expected porosity of our ligand-free nc-Si CNA, it was important to compare the rates of reactive ion etching of these materials to established standards (e.g., a-Si, sc-Si). Silicon thin films have an extensive use in the semiconductor industry where they undergo different steps of etching and doping to finally create a transistor or other devices.

A schematic of the Reactive Ion Etching experiment is shown in Figure 3. The thin films were exposed to SF₆/O₂/Ar plasma in conditions (18:10:10.6 SCCM for SF₆:O₂:Ar; 10W power; 10 mTorr) calibrated to yield a 27.1 nm/min etch rate on sc-Si. An aluminum hard mask with open slots (cf. Fig 3a) was placed on top of the ligand-free CNAs during RIE. The thickness of the exposed and unexposed areas was compared to extract a rate of etching. Due to the small thickness of the films, the high etch rate of SF₆, and the timescales of the RIE process, we were only able to collect one time point at 90s. Figure 3b shows the SEM micrographs of the exposed and unexposed areas of the ncSi films after RIE. The films decrease visibly in thickness, but the surface does not seem to develop new defects – cracking was not observed as a result of RIE.

An important question regarding etching in these porous systems is whether it is primarily driven by ions or whether, due to the high porosity of the films, long lived excited species contribute to the process, as in the case of the etching of the ligands. To begin to answer this question, we measured the etch rate as a function of the size of the Si nanoparticles. The rate of etching, in a zeroth-order approximation, should be proportional to the area of the exposed surface. If anisotropic etching dominates, the exposed surface is only the one at the top of the film. Assuming the particles have a spherical shape, and are not arranged in a close-packed lattice – we assume a square arrangement, for simplicity – at the top of the film, the exposed surface is $1+\pi/4 = 1.78$ times the equivalent surface of the flat substrate underneath (cf. Figure 3c). Importantly, within these assumptions, this factor does not change with the size of the particles. If long-lived species contribute, they can access, in principle, the exposed surfaces of all particles in the film. Therefore, the etch rate should be much larger and should increase with increasing surface area of the CNA (i.e., decreasing particle size).

Figure 3d shows the etch rate measured from nc-Si film obtained from particles of different sizes (TEM sizes are used here). The etch rates (red scatters) do not depend significantly on the size of the particles (scatter in the data is attributed to imperfect flatness of the films which caused significant errors, 10-20%, in the thickness measurement), consistently with anisotropic etching. The average etch rate, measured across all sizes of particles is 50.7 nm/min (dashed red line), which is 1.87 times larger than for the sc-Si standard (grey line). This value is consistent with the etch rate expected from the geometric argument described above. Therefore, these results indicate that the increased exposed area at the surface of the film due to the granular nature of the building blocks is the main factor influencing etch rates in this system. Interestingly, according to the model

described above, particle shape should be an important factor in determining RIE etching rates for these films.

Conclusions

In conclusion we have demonstrated a facile strategy for the spin-on preparation of crack-free, carbon-free nanocrystalline silicon thin film by a process involving the scalable synthesis of Si nanocrystals, their spin-coating on a substrate, and the removal of the ligand by plasma etching with He or He/H₂ plasmas. The plasma processed thin films are seen to have about 1.87 times faster reactive ion etch rates than commercial standard single crystalline silicon, which can be attributed to increased roughness of the films. We presented a convenient approach to create thin films of nanocrystalline silicon without the need for high temperature processing.

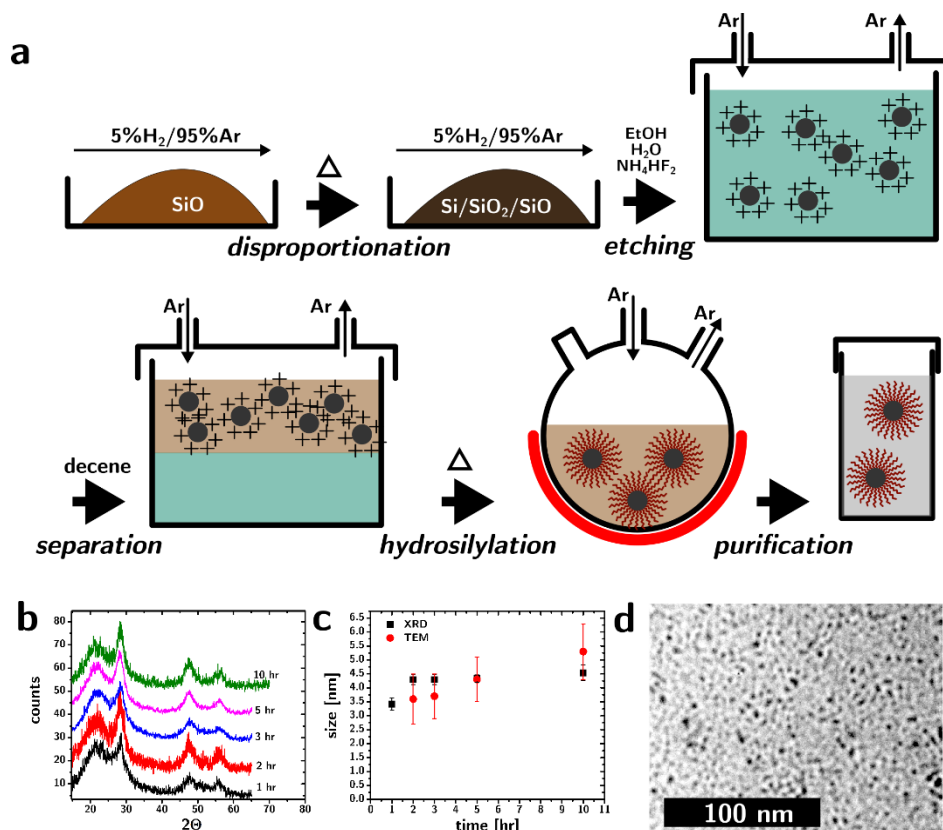


Figure 1. Synthesis and characterization of colloidal Si nanocrystals. **a)** Schematic of the synthesis steps: disproportionation of SiO, liberation of Si nanocrystals, separation into decene, hydrosilylation to form decyl-capped Si nanocrystals, and purification to isolate the nanocrystals in hexane. **b)** XRD of the SiO powder after calcination at 1000 °C in 5% H₂ : 95% Ar atmosphere. **c)** Scherrer-derived (XRD) and TEM-derived particle size distribution showing how the size of the particle is not significantly different from the size of the crystals, indicating high crystallinity. **d)** TEM imaging of the colloidal stabilized nanocrystals.

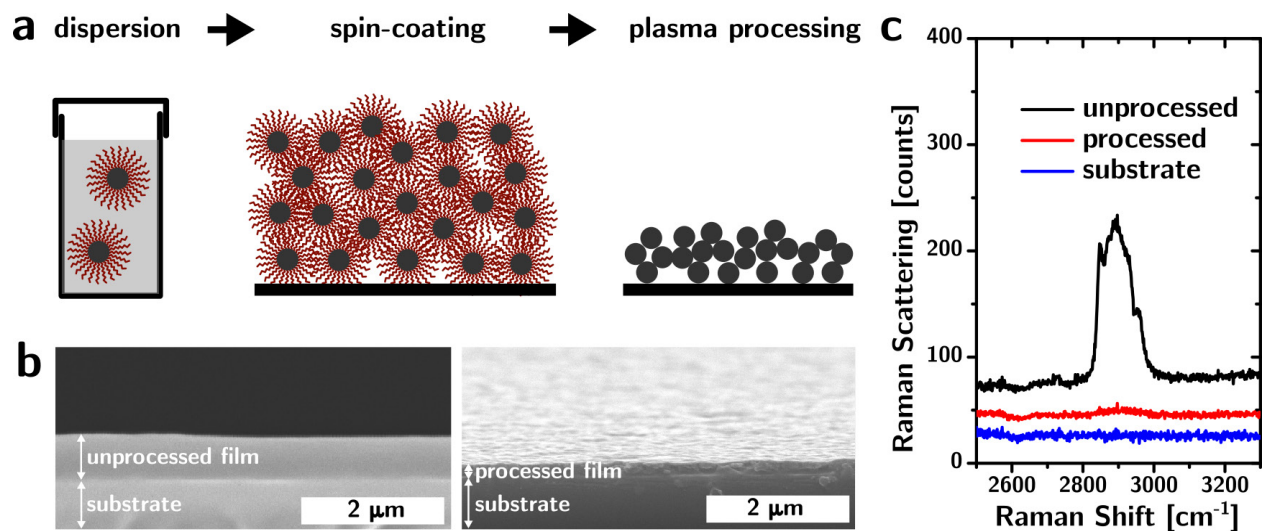


Figure 2. Spin-coating and plasma processing of the films to yield nc-Si films. a) Schematic of the deposition of Si nanocrystals on substrate by spin-coating and subsequent ligand removal by plasma processing. b) SEM of the cross-section of deposited Si film before and after plasma processing. c) Raman spectra of the unprocessed and processed nc-Si films and substrate showing the dramatic decrease of C-H content after exposed to plasma (peak region at 2850 – 2990 cm^{-1}).

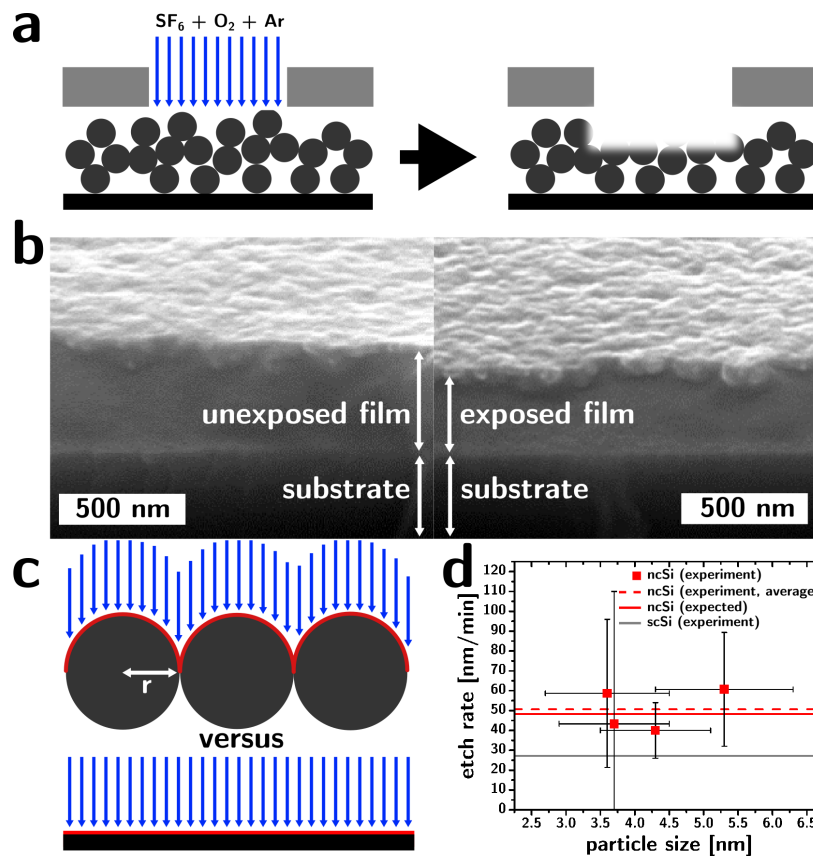


Figure 3. Reactive Ion Etching of spin-on nc-Si films obtained from colloidal Si nanocrystals.

A) Schematic of the experiment to determine etch rates by comparing exposed to unexposed areas of the film. B) Cross-sectional SEM images of the unexposed (left) and exposed (right) regions of the films. C) Schematic demonstration of the effect of nanoscale surface roughness on the etching when compared with a flat surface. D) Etch rate measured from nc-Si film made of different particle size. Dashed red line shows the average etch rate measured across all sizes of particles. Grey line is for the sc-Si standard.

AUTHOR INFORMATION

Corresponding Author

*Email: lcademar@iastate.edu

ACKNOWLEDGMENT

The work described in this paper has been supported by the Member-Specific-Research-Intel program of Semiconductor Research Corporation under Award No. 2015-IN-2582. The Raman measurements were supported by the U.S. Department of Energy, Office of Basic Energy Sciences, Division of Chemical Sciences, Geosciences, and Biosciences through the Ames Laboratory. The Ames Laboratory is operated for the U.S. Department of Energy by Iowa State University under Contract No. DE-AC02-07CH11358.

REFERENCES

- (1) Ali, M.; Zhou, F.; Chen, K.; Kotzur, C.; Xiao, C.; Bourgeois, L.; Zhang, X.; MacFarlane, D. R. Nanostructured photoelectrochemical solar cell for nitrogen reduction using plasmon-enhanced black silicon. *Nat. Commun.* **2016**, *7*, 11335.
- (2) Rao, S.; Prater, J.; Wu, F.; Shelton, C.; Maria, J.-P.; Narayan, J. Interface magnetism in epitaxial BiFeO₃-La_{0.7}Sr_{0.3}MnO₃ heterostructures integrated on Si (100). *Nano Lett.* **2013**, *13*, 5814-5821.
- (3) Shimura, F. Single-Crystal Silicon: Growth and Properties. In *Springer Handbook of Electronic and Photonic Materials*; Kasap, S.; Capper, P., Eds.; Springer US: Boston, MA, 2007; pp 255-269.
- (4) Green, M. A.; Emery, K.; Hishikawa, Y.; Warta, W.; Dunlop, E. D. Solar cell efficiency tables (Version 45). *Progress in photovoltaics: research and applications* **2015**, *23*, 1-9.
- (5) Cousins, P. J.; Smith, D. D.; Luan, H.-C.; Manning, J.; Dennis, T. D.; Waldhauer, A.; Wilson, K. E.; Harley, G.; Mulligan, W. P. In *Generation 3: Improved performance at lower cost*, Photovoltaic Specialists Conference (PVSC), 2010 35th IEEE, IEEE: 2010; pp 000275-000278.
- (6) Priolo, F.; Gregorkiewicz, T.; Galli, M.; Krauss, T. F. Silicon nanostructures for photonics and photovoltaics. *Nat. Nanotechnol.* **2014**, *9*, 19-32.
- (7) Shah, A. Thin-film silicon solar cells. In *McEvoy's Handbook of Photovoltaics (Third Edition)*; Elsevier: 2017; pp 235-307.
- (8) Park, N.-M.; Kim, T.-S.; Park, S.-J. Band gap engineering of amorphous silicon quantum dots for light-emitting diodes. *Appl. Phys. Lett.* **2001**, *78*, 2575-2577.
- (9) Wilson, W. L.; Szajowski, P.; Brus, L. Quantum confinement in size-selected, surface-oxidized silicon nanocrystals. *Science* **1993**, *262*, 1242-1244.
- (10) Kołodziej, A. Staebler-Wronski effect in amorphous silicon and its alloys. *Opto-electronics review* **2004**, *12*, 21-32.
- (11) Xu, S.; Tang, X.; Yue, Y.; Wang, X. Submicron imaging of subsurface nanocrystalline structure in silicon. *J. Raman Spectrosc.* **2013**, *44*, 1523-1528.

- (12) He, Y.; Yin, C.; Cheng, G.; Wang, L.; Liu, X.; Hu, G. The structure and properties of nanosize crystalline silicon films. *J. Appl. Phys.* **1994**, *75*, 797-803.
- (13) Sykora, M.; Mangolini, L.; Schaller, R. D.; Kortshagen, U.; Jurbergs, D.; Klimov, V. I. Size-dependent intrinsic radiative decay rates of silicon nanocrystals at large confinement energies. *Phys. Rev. Lett.* **2008**, *100*, 067401.
- (14) Mangolini, L.; Kortshagen, U. Plasma-Assisted Synthesis of Silicon Nanocrystal Inks. *Adv. Mater.* **2007**, *19*, 2513-2519.
- (15) Jurbergs, D.; Rogojina, E.; Mangolini, L.; Kortshagen, U. Silicon nanocrystals with ensemble quantum yields exceeding 60%. *Appl. Phys. Lett.* **2006**, *88*, 233116.
- (16) Hessel, C. M.; Henderson, E. J.; Veinot, J. G. Hydrogen silsesquioxane: a molecular precursor for nanocrystalline Si–SiO₂ composites and freestanding hydride-surface-terminated silicon nanoparticles. *Chem. Mater.* **2006**, *18*, 6139-6146.
- (17) Hessel, C. M.; Reid, D.; Panthani, M. G.; Rasch, M. R.; Goodfellow, B. W.; Wei, J.; Fujii, H.; Akhavan, V.; Korgel, B. A. Synthesis of ligand-stabilized silicon nanocrystals with size-dependent photoluminescence spanning visible to near-infrared wavelengths. *Chem. Mater.* **2011**, *24*, 393-401.
- (18) Mastronardi, M. L.; Maier-Flaig, F.; Faulkner, D.; Henderson, E. J.; Kübel, C.; Lemmer, U.; Ozin, G. A. Size-dependent absolute quantum yields for size-separated colloiddally-stable silicon nanocrystals. *Nano Lett.* **2011**, *12*, 337-342.
- (19) Mastronardi, M. L.; Henderson, E. J.; Puzzo, D. P.; Ozin, G. A. Small Silicon, Big Opportunities: The Development and Future of Colloiddally-Stable Monodisperse Silicon Nanocrystals. *Adv. Mater. (Weinheim, Ger.)* **2012**, *24*, 5890-5898.
- (20) Lindroos, J.; Savin, H. Review of light-induced degradation in crystalline silicon solar cells. *Sol. Energy Mater. Sol. Cells* **2016**, *147*, 115-126.
- (21) Gresback, R.; Nozaki, T.; Okazaki, K. Synthesis and oxidation of luminescent silicon nanocrystals from silicon tetrachloride by very high frequency nonthermal plasma. *Nanotechnology* **2011**, *22*, 305605.
- (22) Bux, S. K.; Rodriguez, M.; Yeung, M. T.; Yang, C.; Makhluף, A.; Blair, R. G.; Fleurial, J.-P.; Kaner, R. B. Rapid solid-state synthesis of nanostructured silicon. *Chem. Mater.* **2010**, *22*, 2534-2540.
- (23) Terukov, E.; Kudoyarova, V. K.; Davydov, V. Y.; Koughia, K.; Weiser, G.; Mell, H. The influence of deposition parameters on the structure of nanocrystalline silicon. *Materials Science and Engineering: B* **2000**, *69*, 266-271.
- (24) Gabard, M.; Zaghrioui, M.; Chouteau, D.; Grimal, V.; Tillocher, T.; Ghamouss, F.; Poirot, N. Novel Method Based on Spin-Coating for the Preparation of 2D and 3D Si-Based Anodes for Lithium Ion Batteries. *ChemEngineering* **2017**, *1*, 5.
- (25) Drahi, E.; Blayac, S.; Borbely, A.; Benaben, P. Impact of ink synthesis on processing of inkjet-printed silicon nanoparticle thin films: A comparison of Rapid Thermal Annealing and photonic sintering. *Thin Solid Films* **2015**, *574*, 169-176.
- (26) Büchter, B.; Seidel, F.; Fritzsche, R.; Lehmann, D.; Bülz, D.; Buschbeck, R.; Jakob, A.; Schulze, S.; Freitag, H.; Lang, H. Polycrystalline silicon foils by flash lamp annealing of spray-coated silicon nanoparticle dispersions. *J. Mater. Sci.* **2015**, *50*, 6050-6059.
- (27) Shaw, S.; Silva, T. F.; Bobbitt, J. M.; Naab, F.; Rodrigues, C. L.; Yuan, B.; Chang, J. J.; Tian, X.; Smith, E. A.; Cademartiri, L. Building Materials from Colloiddal Nanocrystal Assemblies: Molecular Control of Solid/Solid Interfaces in Nanostructured Tetragonal ZrO₂. *Chem. Mater.* **2017**, *29*, 7888-7900.

- (28) Shaw, S.; Yuan, B.; Tian, X. C.; Miller, K. J.; Cote, B. M.; Colaux, J. L.; Migliori, A.; Panthani, M. G.; Cademartiri, L. Building Materials from Colloidal Nanocrystal Arrays: Preventing Crack Formation During Ligand Removal by Controlling Structure and Solvation. *Adv. Mater. (Weinheim, Ger.)* **2016**, *28*, 8892-8899.
- (29) Shaw, S.; Colaux, J. L.; Hay, J. L.; Peiris, F. C.; Cademartiri, L. Building Materials from Colloidal Nanocrystal Arrays: Evolution of Structure, Composition, and Mechanical Properties Upon Removal of Ligands by O₂ Plasma. *Adv. Mater. (Weinheim, Ger.)* **2016**, *28*, 8900-8905.
- (30) Chernomordik, B. D.; Ketkar, P. M.; Hunter, A. K.; Béland, A. E.; Deng, D. D.; Aydil, E. S. Microstructure Evolution During Selenization of Cu₂ZnSnS₄ Colloidal Nanocrystal Coatings. *Chem. Mater.* **2016**, *28*, 1266-1276.
- (31) Kortshagen, U. R.; Sankaran, R. M.; Pereira, R. N.; Girshick, S. L.; Wu, J. J.; Aydil, E. S. Nonthermal plasma synthesis of nanocrystals: fundamental principles, materials, and applications. *Chem. Rev.* **2016**, *116*, 11061-11127.
- (32) Greenberg, B. L.; Ganguly, S.; Held, J. T.; Kramer, N. J.; Mkhoyan, K. A.; Aydil, E. S.; Kortshagen, U. R. Nonequilibrium-Plasma-Synthesized ZnO Nanocrystals with Plasmon Resonance Tunable via Al Doping and Quantum Confinement. *Nano Lett.* **2015**, *15*, 8162-8169.
- (33) Leschkies, K. S.; Kang, M. S.; Aydil, E. S.; Norris, D. J. Influence of Atmospheric Gases on the Electrical Properties of PbSe Quantum-Dot Films. *J. Phys. Chem. C* **2010**, *114*, 9988-9996.
- (34) Leschkies, K. S.; Beatty, T. J.; Kang, M. S.; Norris, D. J.; Aydil, E. S. Solar Cells Based on Junctions between Colloidal PbSe Nanocrystals and Thin ZnO Films. *ACS Nano* **2009**, *3*, 3638-3648.
- (35) Dolzhenkov, D. S.; Zhang, H.; Jang, J.; Son, J. S.; Panthani, M. G.; Shibata, T.; Chattopadhyay, S.; Talapin, D. V. Composition-matched molecular "solders" for semiconductors. *Science* **2015**, *347*, 425-428.
- (36) Kovalenko, M. V.; Manna, L.; Cabot, A.; Hens, Z.; Talapin, D. V.; Kagan, C. R.; Klimov, V. I.; Rogach, A. L.; Reiss, P.; Milliron, D. J.; Guyot-Sionnest, P.; Konstantatos, G.; Parak, W. J.; Hyeon, T.; Korgel, B. A.; Murray, C. B.; Heiss, W. Prospects of Nanoscience with Nanocrystals. *ACS Nano* **2015**, *9*, 1012-1057.
- (37) Kovalenko, M. V.; Schaller, R. D.; Jarzab, D.; Loi, M. A.; Talapin, D. V. Inorganically Functionalized PbS-CdS Colloidal Nanocrystals: Integration into Amorphous Chalcogenide Glass and Luminescent Properties. *J. Am. Chem. Soc.* **2012**, *134*, 2457-2460.
- (38) Llordés, A.; Garcia, G.; Gazquez, J.; Milliron, D. J. Tunable near-infrared and visible-light transmittance in nanocrystal-in-glass composites. *Nature* **2013**, *500*, 323-326.
- (39) Rosen, E. L.; Buonsanti, R.; Llordés, A.; Sawvel, A. M.; Milliron, D. J.; Helms, B. A. Exceptionally mild reactive stripping of native ligands from nanocrystal surfaces by using Meerwein's salt. *Angewandte Chemie International Edition* **2012**, *51*, 684-689.
- (40) Tangirala, R.; Baker, J. L.; Alivisatos, A. P.; Milliron, D. J. Modular inorganic nanocomposites by conversion of nanocrystal superlattices. *Angew. Chem.* **2010**, *122*, 2940-2944.
- (41) Kinder, E.; Moroz, P.; Diederich, G.; Johnson, A.; Kirsanova, M.; Nemchinov, A.; O'Connor, T.; Roth, D.; Zamkov, M. Fabrication of all-inorganic nanocrystal solids through matrix encapsulation of nanocrystal arrays. *J. Am. Chem. Soc.* **2011**, *133*, 20488-20499.

- (42) Maurer, J. H.; González-García, L.; Reiser, B.; Kanelidis, I.; Kraus, T. Sintering of ultrathin gold nanowires for transparent electronics. *ACS Appl. Mater. Interfaces* **2015**, *7*, 7838-7842.
- (43) Xia, Y. S.; Nguyen, T. D.; Yang, M.; Lee, B.; Santos, A.; Podsiadlo, P.; Tang, Z. Y.; Glotzer, S. C.; Kotov, N. A. Self-assembly of self-limiting monodisperse supraparticles from polydisperse nanoparticles. *Nat. Nanotechnol.* **2011**, *6*, 580-587.
- (44) Niederberger, M.; Cölfen, H. Oriented attachment and mesocrystals: Non-classical crystallization mechanisms based on nanoparticle assembly. *Phys. Chem. Chem. Phys.* **2006**, *8*, 3271-3287.
- (45) Norris, D. J.; Vlasov, Y. A. Chemical approaches to three-dimensional semiconductor photonic crystals. *Adv. Mater. (Weinheim, Ger.)* **2001**, *13*, 371-376.
- (46) Mohapatra, P.; Shaw, S.; Mendivelso-Perez, D.; Bobbitt, J. M.; Silva, T. F.; Naab, F.; Yuan, B.; Tian, X.; Smith, E. A.; Cademartiri, L. Calcination does not remove all carbon from colloidal nanocrystal assemblies. *Nat. Commun.* **2017**, *8*, 2038.
- (47) Cademartiri, L.; Ghadimi, A.; Ozin, G. A. Nanocrystal Plasma Polymerization: From Colloidal Nanocrystals to Inorganic Architectures. *Acc. Chem. Res.* **2008**, *41*, 1820-1830.
- (48) Cademartiri, L.; von Freymann, G.; Arsenault, A. C.; Bertolotti, J.; Wiersma, D. S.; Kitaev, V.; Ozin, G. A. Nanocrystals as precursors for flexible functional films. *Small* **2005**, *1*, 1184-1187.
- (49) Shaw, S.; Tian, X. C.; Silva, T. F.; Bobbitt, J.; Rodrigues, C.; Naab, F.; Hamdeh, H.; Panthani, M. G.; Smith, E. A.; Cademartiri, L. Highly Conductive Colloidal Nanocrystal Assemblies By The Selective Removal Of Ligands With Non-Oxidizing He Plasmas. **2018**, submitted.
- (50) Intartaglia, R.; Bagga, K.; Scotto, M.; Diaspro, A.; Brandi, F. Luminescent silicon nanoparticles prepared by ultra short pulsed laser ablation in liquid for imaging applications. *Optical Materials Express* **2012**, *2*, 510-518.
- (51) Wang, Y.-L.; Xu, W.; Zhou, Y.; Chu, L.-Z.; Fu, G.-S. Influence of pulse repetition rate on the average size of silicon nanoparticles deposited by laser ablation. *Laser Part. Beams* **2007**, *25*, 9-13.
- (52) Yoshida, T.; Takeyama, S.; Yamada, Y.; Mutoh, K. Nanometer-sized silicon crystallites prepared by excimer laser ablation in constant pressure inert gas. *Appl. Phys. Lett.* **1996**, *68*, 1772-1774.
- (53) Lam, C.; Zhang, Y.; Tang, Y.; Lee, C.; Bello, I.; Lee, S. Large-scale synthesis of ultrafine Si nanoparticles by ball milling. *J. Cryst. Growth* **2000**, *220*, 466-470.
- (54) Erogbogbo, F.; Yong, K.-T.; Hu, R.; Law, W.-C.; Ding, H.; Chang, C.-W.; Prasad, P. N.; Swihart, M. T. Biocompatible magnetofluorescent probes: luminescent silicon quantum dots coupled with superparamagnetic iron (III) oxide. *ACS Nano* **2010**, *4*, 5131-5138.
- (55) Sudeep, P.K.; Page, Z.; Emrick, T. PEGylated silicon nanoparticles: synthesis and characterization. *Chem. Commun.* **2008**, *0*, 6126-6127.
- (56) Mangolini, L.; Thimsen, E.; Kortshagen, U. High-yield plasma synthesis of luminescent silicon nanocrystals. *Nano Lett.* **2005**, *5*, 655-659.
- (57) Veinot, J. G. C. Synthesis, surface functionalization, and properties of freestanding silicon nanocrystals. *Chem. Commun.* **2006**, *0*, 4160-4168.
- (58) Yu, Y.; Rowland, C. E.; Schaller, R. D.; Korgel, B. A. Synthesis and ligand exchange of thiol-capped silicon nanocrystals. *Langmuir* **2015**, *31*, 6886-6893.

- (59) Sun, W.; Qian, C.; Cui, X. S.; Wang, L.; Wei, M.; Casillas, G.; Helmy, A. S.; Ozin, G. A. Silicon monoxide—a convenient precursor for large scale synthesis of near infrared emitting monodisperse silicon nanocrystals. *Nanoscale* **2016**, *8*, 3678-3684.
- (60) Gunduz, D. C.; Tankut, A.; Sedani, S.; Karaman, M.; Turan, R. Crystallization and phase separation mechanism of silicon oxide thin films fabricated via e-beam evaporation of silicon monoxide. *physica status solidi (c)* **2015**, *12*, 1229-1235.
- (61) Mellor, J. W. *A comprehensive treatise on inorganic and theoretical chemistry*, Longmans, Green and Co: 1946.
- (62) Yasaitis, J. A.; Kaplow, R. Structure of amorphous silicon monoxide. *J. Appl. Phys.* **1972**, *43*, 995-1000.
- (63) Friede, B.; Jansen, M. Some comments on so-called 'silicon monoxide'. *J. Non-Cryst. Solids* **1996**, *204*, 202-203.
- (64) Schulmeister, K.; Mader, W. TEM investigation on the structure of amorphous silicon monoxide. *J. Non-Cryst. Solids* **2003**, *320*, 143-150.
- (65) Hirata, A.; Kohara, S.; Asada, T.; Arao, M.; Yogi, C.; Imai, H.; Tan, Y.; Fujita, T.; Chen, M. Atomic-scale disproportionation in amorphous silicon monoxide. *Nat. Commun.* **2016**, *7*, 11591-11597.
- (66) Sepehri-Amin, H.; Ohkubo, T.; Kodzuka, M.; Yamamura, H.; Saito, T.; Iba, H.; Hono, K. Evidence for nano-Si clusters in amorphous SiO anode materials for rechargeable Li-ion batteries. *Scr. Mater.* **2013**, *69*, 92-95.
- (67) Hohl, A.; Wieder, T.; Van Aken, P.; Weirich, T.; Denninger, G.; Vidal, M.; Oswald, S.; Deneke, C.; Mayer, J.; Fuess, H. An interface clusters mixture model for the structure of amorphous silicon monoxide (SiO). *J. Non-Cryst. Solids* **2003**, *320*, 255-280.
- (68) Li, Y.; Liang, P.; Hu, Z.; Guo, S.; You, Q.; Sun, J.; Xu, N.; Wu, J. Enhancement and stability of photoluminescence from Si nanocrystals embedded in a SiO₂ matrix by H₂-passivation. *Appl. Surf. Sci.* **2014**, *300*, 178-183.
- (69) Borrero-González, L.; Nunes, L. A. O.; Andreetta, M. R. B.; Wojcik, J.; Mascher, P.; Pusep, Y. A.; Comedi, D.; Guimarães, F. E. G. The role of quantum confinement and crystalline structure on excitonic lifetimes in silicon nanoclusters. *J. Appl. Phys.* **2010**, *108*, 013105.
- (70) Langford, J. I.; Wilson, A. J. C. Sherrer after Sixty Years: A Survey and Some New Results in the Determination of Crystallite Size. *J. Appl. Crystallogr.* **1978**, *11*, 102-113.
- (71) Cademartiri, L.; Montanari, E.; Calestani, G.; Migliori, A.; Guagliardi, A.; Ozin, G. A. Size-dependent extinction coefficients of PbS quantum dots. *J. Am. Chem. Soc.* **2006**, *128*, 10337-10346.
- (72) Sun, W.; Qian, C.; Mastronardi, M. L.; Wei, M.; Ozin, G. A. Hydrosilylation kinetics of silicon nanocrystals. *Chem. Commun. (Cambridge, U. K.)* **2013**, *49*, 11361-11363.
- (73) Talapin, D. V.; Rogach, A. L.; Haase, M.; Weller, H. Evolution of an ensemble of nanoparticles in a colloidal solution: Theoretical study. *J. Phys. Chem. B* **2001**, *105*, 12278-12285.
- (74) Han, L.; Xin, Y.; Liu, H.; Ma, X.; Tang, G. Photoelectrocatalytic properties of nitrogen doped TiO₂/Ti photoelectrode prepared by plasma based ion implantation under visible light. *J. Hazard. Mater.* **2010**, *175*, 524-531.
- (75) Depla, D.; Colpaert, A.; Eufinger, K.; Segers, A.; Haemers, J.; De Gryse, R. Target voltage behaviour during DC sputtering of silicon in an argon/nitrogen mixture. *Vacuum* **2002**, *66*, 9-17.